Modeling Land Surface Processes and Heavy Rainfall in Urban Environments: Sensitivity to Urban Surface Representations

DAN LI, ELIE BOU-ZEID, AND MARY LYNN BAECK

Department of Civil and Environmental Engineering, Princeton University, Princeton, New Jersey

STEPHEN JESSUP

Department of Civil and Environmental Engineering, Princeton University, Princeton, New Jersey, and Department of Earth and Atmospheric Sciences, Cornell University, Ithaca, New York

JAMES A. SMITH

Department of Civil and Environmental Engineering, Princeton University, Princeton, New Jersey

(Manuscript received 25 October 2012, in final form 8 January 2013)

ABSTRACT

High-resolution simulations with the Weather Research and Forecasting Model (WRF) are used in conjunction with observational analyses to investigate land surface processes and heavy rainfall over the Baltimore–Washington metropolitan area. Analyses focus on a 6-day period, 21–26 July 2008, which includes a major convective rain event (23–24 July), a prestorm period (21–22 July), and a dry-down period (25–26 July). The performance of WRF in capturing land–atmosphere interactions, the bulk structure of the atmospheric boundary layer, and the rainfall pattern in urban environments is explored. Results indicate that WRF captures the incoming radiative fluxes and surface meteorological conditions. Mean profiles of potential temperature and humidity in the atmosphere are also relatively well reproduced, both preceding and following the heavy rainfall period. However, wind features in the lower atmosphere, including low-level jets, are not accurately reproduced by WRF. The biases in the wind fields play a central role in determining errors in WRF-simulated rainfall fields. The study also investigates the sensitivity of WRF simulations to different urban surface representations. It is found that urban surface representations have a significant impact on the surface energy balance and the rainfall distribution. As the impervious fraction increases, the sensible heat flux and the ground heat flux increase, while the latent heat flux decreases. The impact of urban surface representations on precipitation is as significant as that of microphysical parameterizations. The fact that changing urban surface representations can significantly alter the rainfall field suggests that urbanization plays an important role in modifying the regional precipitation pattern.

1. Introduction

Precipitation is the primary driver of land surface hydrological processes and the main component of the terrestrial water budget (Brutsaert 2005). It also affects the surface energy budget and land–atmosphere interactions by modifying soil moisture (Betts et al. 1996). High-resolution modeling of land surface hydrological processes enabled by the ever-increasing computing power requires detailed rainfall estimates as inputs (Wood et al. 2011). However, physically based rainfall modeling remains a significant challenge, particularly because of the strong and complex interactions between synoptic forcing, microphysical processes, land–atmosphere exchanges, and the evolution of the atmospheric boundary layer (Pielke 2001; Shephard 2005; Trier et al. 2011; Yeung et al. 2011).

The impact of land–atmosphere exchanges and atmospheric boundary layer processes on warm season rainfall is the subject of active research (Trier et al. 2004, 2008, 2011), including a number of studies with a specific focus on urban environments (Shephard 2005; Ntelekos et al. 2007, 2008; Miao et al. 2011; Niyogi et al. 2011;

Corresponding author address: Dan Li, Department of Civil and Environmental Engineering, Princeton University, 59 Olden St., Princeton, NJ 08544.
E-mail: danl@princeton.edu

DOI: 10.1175/JHM-D-12-0154.1

Yeung et al. 2011). In this study, the Weather Research and Forecasting Model (WRF) is used to investigate the interactions between land–atmosphere exchanges, boundary layer processes, and heavy rainfall in the Baltimore–Washington metropolitan region, where heavy rainfall is often observed to be associated with organized thunderstorm systems and induces heavy flooding (Ntelekos et al. 2007, 2008; Zhang et al. 2009).

WRF is a community model and has multiple parameterization schemes for each of its five physical packages: cumulus clouds, microphysics, radiation, planetary boundary layer (PBL), and the surface (Skamarock and Klemp 2008). Studies have demonstrated that some of the physics schemes can significantly affect rainfall modeling. For example, Jankov et al. (2005) analyzed the sensitivity of warm-season mesoscale convective system rainfall to different physical parameterizations and concluded that the microphysics and the PBL schemes have relatively larger impacts than the cumulus schemes. Trier et al. (2004, 2008, 2011) investigated the impact of land surface processes, including surface energy partitioning and changes in soil conditions, on convection initiation and warm-season precipitation. In this study, we primarily explore the sensitivity of heavy rainfall in WRF to different urban surface representations by developing a better understanding of the linkages between land–atmosphere exchanges, boundary layer processes, and heavy rainfall. We also examine the sensitivity of model simulations of rainfall to microphysical parameterizations and use the sensitivity to microphysical parameterizations as a reference to compare with the sensitivity to urban surface representations.

The urban surface representation is an important element to examine because many previous studies have demonstrated the impact of urbanization on the surface energy balance and rainfall climatology [see Shephard (2005) for a review and Smith et al. (2012) for analyses in the Baltimore study region]. Three main mechanisms that are responsible for urban modification of precipitation are urban heat island effects (e.g., Bornstein and Lin 2000; Dixon and Mote 2003; Lin et al. 2011), urban canopy effects (e.g., Loose and Bornstein 1977; Miao et al. 2011; Zhang et al. 2011), and urban aerosol effects (e.g., Rosenfeld 2000; Jin and Shepherd 2008; Ntelekos et al. 2009; Jin et al. 2010). Many studies have also demonstrated the significant role of urbanization in modifying storm properties at various urban locations such as New York (Loose and Bornstein 1977), the Baltimore–Washington metropolitan area (Ntelekos et al. 2007), Atlanta (Bornstein and Lin 2000; Shem and Shepherd 2009; Wright et al. 2012), Houston (Shepherd et al. 2010), and a range of cities in the southern United States (Ashley et al. 2012). Urbanization is shown to affect the initiation (e.g., Shepherd et al. 2010), bifurcation (e.g., Bornstein and Lin 2000), and development (e.g., Loose and Bornstein 1977) of storms. Most of these studies have relied on numerical tools such as the WRF model, which can be used with different urban surface representations (Shem and Shepherd 2009; Lee et al. 2011; Miao et al. 2011; Yeung et al. 2011; Zhang et al. 2011). However, there has been no systematic investigation of the impact of these diverse urban surface representations, especially on heavy rainfall modeling. In this study, two aspects of the urban surface representations are investigated: 1) the method for calculating the surface fluxes in urban areas and 2) the land-cover dataset. Traditionally, urban areas have been treated similarly to other land-use categories, but with urban-specific (i.e., impervious surface) parameters. In WRF, the Noah Land Surface Model (Noah LSM) can represent urban terrain using this traditional approach. Nevertheless, over the past decade, there have been many efforts to develop surface modules specifically for urban areas (see, e.g., Wang et al. 2011, 2013). These modules are commonly referred to as urban canopy models (UCMs), and several have been coupled to the Noah LSM in WRF (see Chen et al. 2011 for a review). In our study, the single-layer UCM in WRF is used and further improved. The improved UCM is referred to as the new UCM. Two land-cover datasets are employed in the study: the National Land Cover Data (NLCD) 2006 and the default U.S. Geological Survey (USGS) land-cover dataset that was compiled around 1993 but is still widely used in many WRF studies [some of the studies that have used USGS, at least partially, include Ntelekos et al. (2007); Jiang et al. (2008); Ntelekos et al. (2008); Zhang et al. (2009); Yeung et al. (2011); Talbot et al. (2012)].

In this study, simulations with different urban flux calculation methods (no UCM or the traditional approach, default UCM, and new UCM) and the two land-cover datasets (NLCD2006 and USGS) are intercompared in order to evaluate the impact of urban surface representations on land–atmosphere exchanges and heavy rainfall. In particular, we are focused on the linkages between surface states, atmospheric boundary layer processes, and rainfall within the context of urban environments. The objectives of this study are 1) to assess the performance of WRF in modeling land surface and atmospheric boundary layer processes during a period that includes a major rain event and 2) to test the sensitivity of WRF, and its simulation skill, to different urban surface representations. The paper is organized as follows. In section 2, we introduce the basics of WRF and the observational datasets and describe the selected case briefly. In section 3, we present the main results and comparisons between the simulations and the measurements. A summary and conclusions are presented in section 4.

2. Methodology and data

a. Study area and WRF setup

The WRF simulations in this work are performed over the Baltimore–Washington metropolitan area using three nested domains with horizontal grid spacings of 9, 3, and 1 km. As shown in Fig. 1, the largest domain (d01) covers most of the northeastern United States. The second domain (d02) includes Philadelphia, Pennsylvania; Washington, D.C.; and most of Maryland. The third domain (d03) covers the Baltimore, Maryland, metropolitan area and a portion of the Washington, D.C., metropolitan area. The three domains have 100, 106, and 106 horizontal grid cells, respectively, in the x (east–west) and y (north–south) directions. All domains are centered at the Cub Hill meteorological tower (39.413°N, 76.522°W) and have 109 vertical levels. The vertical levels are stretched and the number of vertical levels is significantly increased compared to some previous studies, particularly in the lower atmosphere, in order to resolve the variability within the atmospheric boundary layer (Talbot et al. 2012).

WRF is a nonhydrostatic model and solves the conservation equations of mass, momentum, and energy on terrain-following coordinates. In this study, WRF version 3.3 is used. Table 1 lists the five simulations that have different combinations of physics parameterization schemes. Four cases are used to illustrate the impact of different urban surface representations: case 1 (the reference simulation) uses the default UCM and case 3 uses the new UCM, both of which are based on the NLCD2006 dataset. Case 4 uses the default UCM with the USGS land-cover dataset. Case 5 does not use a UCM and uses the NLCD2006 dataset. For each grid cell, WRF only considers the dominant land-use category and treats the grid cell as if it is completely composed of that land use. If the dominant land-use category is not ''urban,'' the Noah LSM is called to compute the surface fluxes. For an urban grid cell, the calculation of surface fluxes depends on whether a UCM is used or not. When a UCM is not used, the grid cell is treated as 100% impervious (with urban properties) by the Noah LSM (i.e., the traditional approach). When a UCM is used, the grid cell is treated as a combination of impervious and vegetated surfaces (assumed to be grassland). The Noah LSM is called first to handle the surface–subsurface processes for the vegetated surface, and then the UCM is called to calculate the fluxes from the impervious surface.

Some land-cover datasets, such as the NLCD2006, can provide multiple urban types (e.g., low-density residential, high-density residential, and commercial). Any grid cell whose dominant land-use category is one of these urban types will be considered as an urban grid. The grid cell is still treated as if it is solely composed of that dominant urban land cover. For example, a grid cell that includes 25% of open water surfaces, 25% high-residential urban and 50% commercial urban will be considered as if it is composed of 100% commercial urban. The current WRF-UCM framework is capable of distinguishing three urban categories: low-density residential, high-density residential, and commercial. But when a UCM is not used, the three urban categories are not distinguished. The NLCD 2006 (with 30-m spatial resolution) has four urban categories, which can be reclassified into the three urban categories required by the UCM (see, e.g., Jiang et al. 2008; Zhang et al. 2011). However, the USGS land-cover dataset has only one urban category, which is treated as high-density residential by the UCM.

As mentioned earlier, when a UCM is used, any urban grid cell (i.e., the dominant land-use category is one of the urban types) is treated as a combination of impervious and vegetation surfaces. The partition of the grid cell into impervious fraction and vegetation fraction differs for the three urban categories. The default impervious fractions that are used in the default UCM are 50% for low-density residential urban, 90% for high-density residential urban, and 95% for commercial urban, with the remainder being the vegetation fraction. Not only is the partition of the grid cell into impervious and vegetation fractions different for the three urban categories, the urban canyon configurations and surface properties are also different. For instance, a commercial urban grid cell will have higher buildings than grid cells of the other two urban types. The new UCM that we implemented into WRF still only considers the dominant urban category in each urban cell, but it calculates the impervious fraction directly from the land-cover dataset instead of using the default values.

In summary, when a UCM is used with the NLCD2006 dataset, WRF has three urban categories, with each urban category having different properties and a different impervious surface fraction (the default UCM will use the default values for the impervious surface fractions and the new UCM will calculate the impervious surface fractions from the land-cover dataset). When a UCM is used with the USGS land-cover dataset, WRF only has a single urban category with an impervious surface fraction of 90% and properties of ''high-density

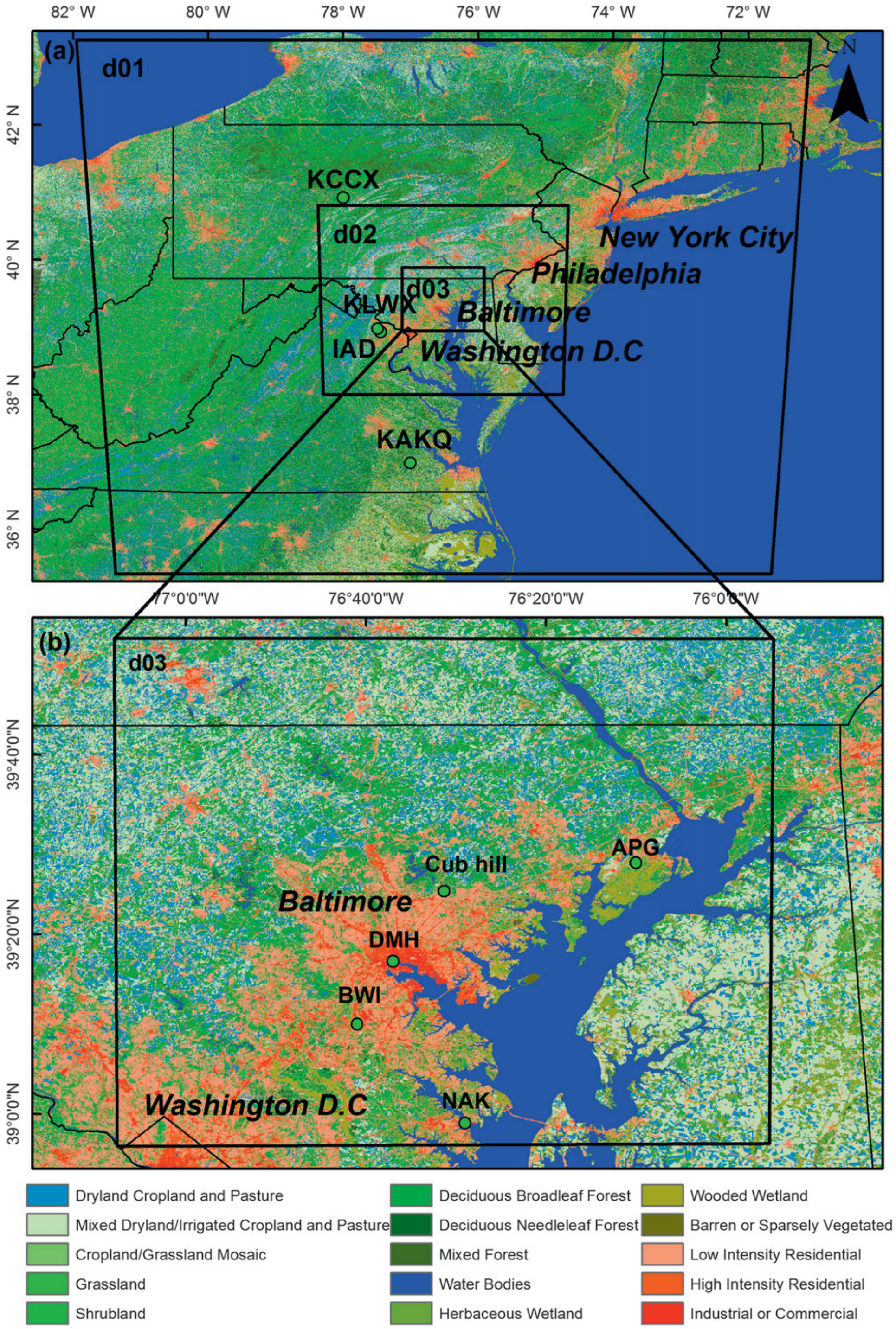

FIG. 1. The land-cover map based on the NLCD 2006 dataset, the WRF domains, and the observational sites over the study area.

urban.'' As a result, although the USGS land-cover dataset is out of date and the total number of urban grids is less than in the NLCD2006, it can have a larger impervious surface fraction in some of the urban grids than the NLCD2006.

To determine whether WRF-simulated rainfall fields are sensitive to the urban surface representations, a reference is needed. In this study, the difference between WRF-simulated rainfall structures using the two microphysics schemes serves as a reference to compare

TABLE 1. Basic information of the WRF simulations.

	Microphysics schemes	Urban canopy model	Land-cover datasets	Urban categories	Impervious fraction of an urban grid cell (%)
1	WSM6	Yes	NLCD2006	3	95, 90, 50
2	WDM6	Yes	NLCD2006	3	95, 90, 50
3	WSM6	Yes (new)	NLCD2006	3	To be calculated
4	WSM6	Yes	USGS	1	90
5	WSM6	No	NLCD2006	3	100

with the sensitivity to urban surface representations. The two microphysics schemes chosen to test in this study are the WRF Single-Moment 6-Class (WSM6) scheme (Hong and Lim 2006) and the WRF Double-Moment 6-Class (WDM6) scheme (Lim and Hong 2010). The six prognostic water substance variables in both of the two schemes are the mixing ratios of water vapor, cloud water, cloud ice, snow, rain, and graupel (Hong and Lim 2006). The WDM6 scheme has additional prognostic variables including the number concentrations of cloud water and rain, as well as the cloud condensation nuclei, so that the aerosol effect on clouds and precipitation can be examined (Lim and Hong 2010). Lim and Hong (2010) reported significant differences in the hydrometeor distributions and the rainfall pattern between the two schemes in simulating an idealized thunderstorm. Later, Hong et al. (2010) evaluated the two microphysics schemes by studying two real cases: a squall line over the U.S. Great Plains and a summer monsoon rainfall event over East Asia. They concluded that the reflectivity fields and the rainfall fields for both cases are significantly sensitive to the microphysics schemes. As such, if the sensitivity of rainfall to urban surface representations is comparable to the sensitivity to the microphysics schemes, then it can be concluded that rainfall is also significantly sensitive to the urban surface representations.

Other physical parameterization schemes that were selected and not changed include 1) the RRTM scheme for longwave radiation, 2) the Dudhia scheme for shortwave radiation, 3) the Yonsei University (YSU) PBL scheme for vertical diffusion and the 2D Smagorinsky scheme for horizontal diffusion, and 4) the Noah LSM. Cumulus parameterization was not used for any of these domains since even the largest grid size is less than 10 km. In this study, one-way nesting is used. The initial and boundary conditions are taken from the North American Regional Reanalysis (NARR). The simulations all started at 0000 UTC 21 July 2008 and ended at 0000 UTC on 26 July 2008, with an output frequency of 1 h. The time steps for the three domains are 25 s, 25/3 s and 25/9 s, respectively.

b. Observations

In this study, a variety of observational datasets are used to assess the performance of WRF, including:

1) Meteorological variables measured at the Cub Hill tower;
2) The 2-m air temperature and specific humidity measured by the Automated Surface Observing Systems (ASOS) at Baltimore/Washington International Airport (BWI), at the Maryland Science Center (DMH) in downtown Baltimore, and at Annapolis, Maryland (NAK);
3) Sounding profiles measured at the Aberdeen Proving Ground (APG);
4) Vertical profiles of temperature and humidity in the lower atmosphere measured at Dulles International Airport (IAD) and BWI through commercial aircraft observations from the Aircraft Communications Addressing and Reporting System (ACARS);
5) Velocity–azimuth display (VAD) wind profiles from the Weather Surveillance Radar-1988 Doppler (WSR-88D) radars at Richmond, Virginia (KAKQ); Sterling, Virginia (KLWX); and State College, Pennsylvania (KCCX);
6) Hydro–Next Generation Weather Radar (Hydro-NEXRAD) rainfall estimates from the WSR-88D at KLWX (Krajewski et al. 2011; Smith et al. 2012).

All of the observation sites are shown on Fig. 1. Note that IAD is only 6 km southeast of KLWX; thus, the two markers are not individually distinguishable on Fig. 1.

Measurements of the four components of surface radiation, as well as the ground heat flux (G) are available at the Cub Hill tower. Air temperature, specific humidity, wind speed, and wind direction at the top of the Cub Hill tower (41.2 m above the ground level) are also measured by the CS500 temperature and relative humidity probe and the R.M. Young Wind Sentry Anemometer (both Campbell Scientific, Inc., products) at hourly intervals. The sounding profiles at APG were measured once per day during this period, which was at 1200 UTC (0700 LST). The ACARS dataset has multiple measurements per day, but the frequency of measurements depends on the number of flights with installed meteorological instruments. To facilitate the comparison of WRF model outputs to the ACARS data, the ACARS data are interpolated at hourly intervals. The VAD wind profiles from the KAKQ, KLWX, and KCCX radar measurements are interpolated to hourly intervals and 250-m spatial vertical intervals for comparison with WRF model fields.

The rainfall estimates are taken from a long-term, high-resolution radar rainfall dataset (Smith et al. 2012), which is largely based on reflectivity observations from the WSR-88D radar in Sterling, Virginia (KLWX). The reflectivity observations are converted to rainfall rate through the default National Weather Service (NWS) "Z–R relationship":

$$R = 0.017Z^{0.714}, \tag{1}$$

where Z is the radar reflectivity factor ($\mathrm{mm^6\,m^{-3}}$) and R is rainfall rate ($\mathrm{mm\,h^{-1}}$). The resulting rainfall field is then bias corrected using rain gauge observations (Smith et al. 2012). The final dataset covers a large part of the Baltimore metropolitan area (roughly comparable to d03 in the WRF simulations, as shown in Fig. 1) and has a temporal resolution of 15 min and a spatial resolution of 1 km.

c. *Selected case*

The case study period extends from 21 to 26 July 2008. Three periods are distinguished: a prestorm period (from 0000 UTC 21 July to 0000 UTC 22 July), a storm period with heavy rainfall (from 0000 UTC 22 July to 1200 UTC 24 July), and a poststorm period (from 1200 UTC 24 July to 0000 UTC 26 July). Fig. 2 shows the synoptic conditions (i.e., temperature, geopotential height, and wind field at 850 hPa) at four times during the storm period. A low pressure system moves over the Baltimore–Washington metropolitan area from northwest to northeast. As indicated by a temperature gradient and wind shift at 0000 UTC 24 July (Fig. 2c), a cold front is present right across the Baltimore–Washington metropolitan area. Ahead of the cold front, the southerly flow transports moisture into this region (see Fig. 2b). In the following analyses, we will investigate the performance of WRF in capturing these key synoptic features, particularly the frontal boundary and the southerly flow that includes low-level jet (LLJ) features (see Zhang et al. 2006 for related analyses). Although understanding the impact of urban surface representation on heavy rainfall simulation is a central theme of this study, we are also interested in the effect of urban surface representations on land–atmosphere interactions and the atmospheric boundary layer processes under both rainy and nonrainy conditions. In particular, we are focused on the linkages between surface states and fluxes, atmospheric boundary layer processes, and rainfall. As such, we start by examining surface fluxes and boundary layer profiles and subsequently discuss the rainfall modeling.

3. Results and discussions

a. *Energy balance and meteorological conditions near the surface*

In this section, observations of surface radiation, ground heat flux, and mean meteorological variables at the Cub Hill tower are compared to WRF simulation results. The urban representations in the WRF–Noah–UCM framework will be the primary focus since the Cub Hill tower is located downwind of Baltimore City and is surrounded by low-intensity residential surfaces (Fig. 1).

As can be seen from Fig. 3, the incoming shortwave radiation matches the measurements rather well, even during the heavy rainfall event (i.e., on 23 and 24 July; see Fig. 11). WRF also captures the general variations in the incoming longwave radiation, but the discrepancies can be as large as 50 $\mathrm{W\,m^{-2}}$. It is interesting to note that these large discrepancies occur on a clear day (25 July) in the dry-down period. This is probably due to the fact that WRF does not reproduce the correct water vapor profiles in the atmosphere on that day, as will be shown later. The sensitivities of these incoming radiation components to urban surface representations are not substantial. Small variations are observed among simulations with the four urban surface representations, most likely because of their different impacts on land–atmosphere interactions and, hence, on the atmospheric states.

WRF systematically underestimates the net radiation at Cub Hill, especially at noon when net radiation peaks. This is primarily caused by the large surface albedo value currently used for the grid cell where the Cub Hill tower is located. The albedo calculated from the measurements at Cub Hill is approximately 0.1–0.12. However, for any of the four urban surface representations, the albedo value used in WRF is larger than 0.12. For example, when a UCM is not used, any urban grid has an albedo value equal to 0.15. When a UCM is used, the albedo values for both impervious surface and vegetated surface are larger than 0.12: the albedos of the three urban components (i.e., roof, wall, and ground) are 0.2 (although the net urban albedo including canyon radiative trapping effects can be lower) and the albedo of grassland in WRF ranges from 0.18 to 0.23. Consequently, any of the urban surface representations in WRF examined in this study inevitably yields a larger average surface albedo than the one measured at Cub

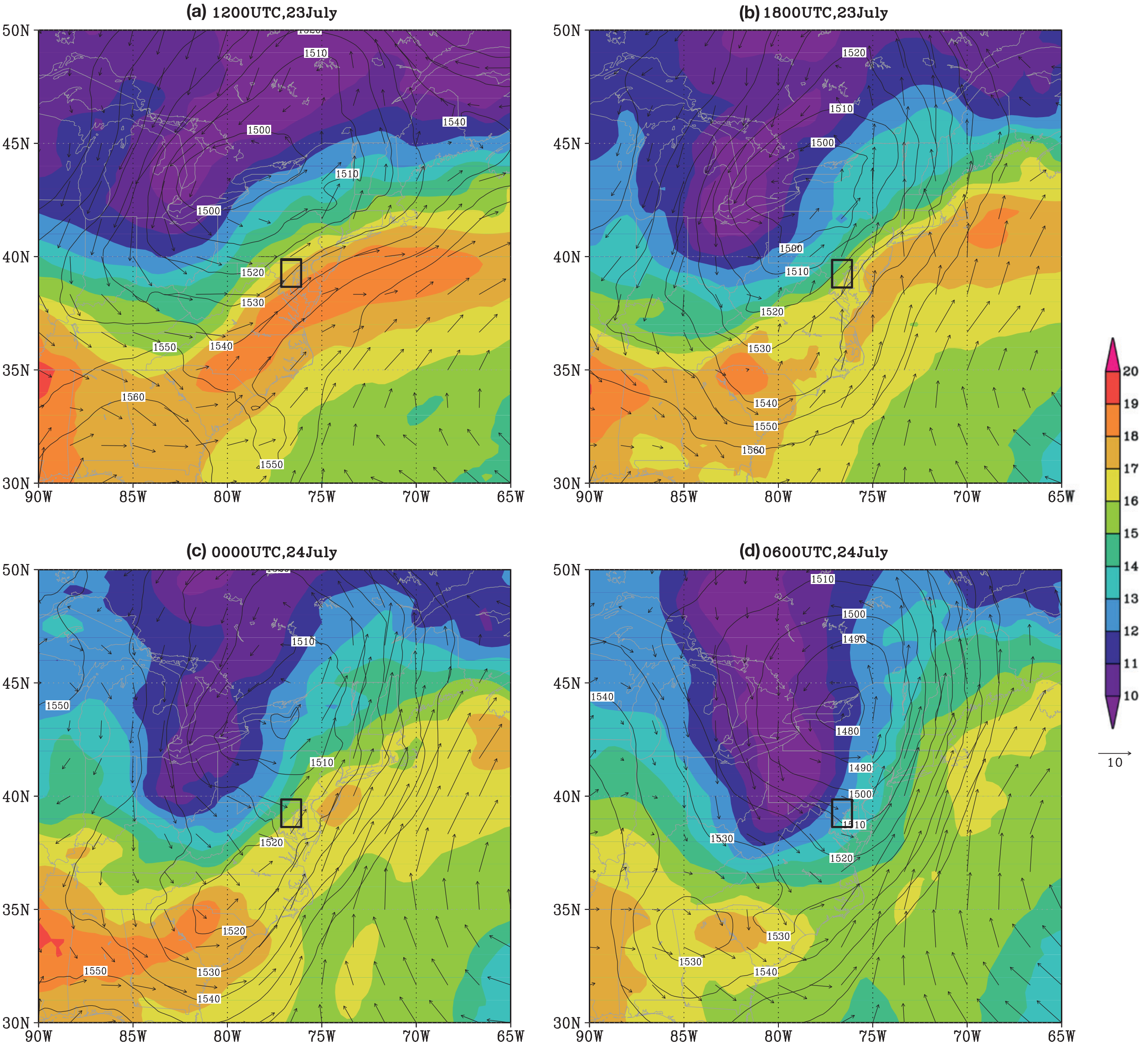

FIG. 2. The synoptic weather patterns at 850 hPa for (a) 1200 UTC 23 Jul, (b) 1800 UTC 23 Jul, (c) 0000 UTC 24 Jul, and (d) 0600 UTC 24 Jul. The shaded color indicates air temperature (°C), the contours denote geopotential height (m), and the arrows denote wind fields (m s^{-1}). The data are taken from NARR. The black squares indicate the Baltimore–Washington metropolitan area (identical to d03 in Fig. 1).

Hill, which leads to lower net radiation, especially during the midday when the incoming solar radiation is large. This underlines the importance of characterizing the surface–soil properties accurately, though this remains a considerable challenge for the highly heterogeneous and diverse urban surfaces.

The surface energy partitioning is particularly sensitive to urban surface representations, as can be seen from the comparisons of ground heat flux (G), sensible heat flux (H), and latent heat flux (LE). Note that no anthropogenic sensible heat flux is included in our simulations. As the urban fraction increases from 50% for the UCM simulation (case 1 in Table 1) to 74% for the UCM (new) simulation (case 3), to 90% for the UCM (USGS) simulation (case 4), and to 100% for the no-UCM simulation (case 5), the daytime ground heat flux and sensible heat flux increase, while the latent heat flux decreases as expected. This illustrates the fact that the impervious/vegetated fraction is a key input parameter for capturing urban surface energy balance. It might appear surprising that the simulation using the out-of-date USGS land-cover dataset produces higher sensible heat fluxes in an urban area than the other two simulations using the more recent NLCD2006 land-cover

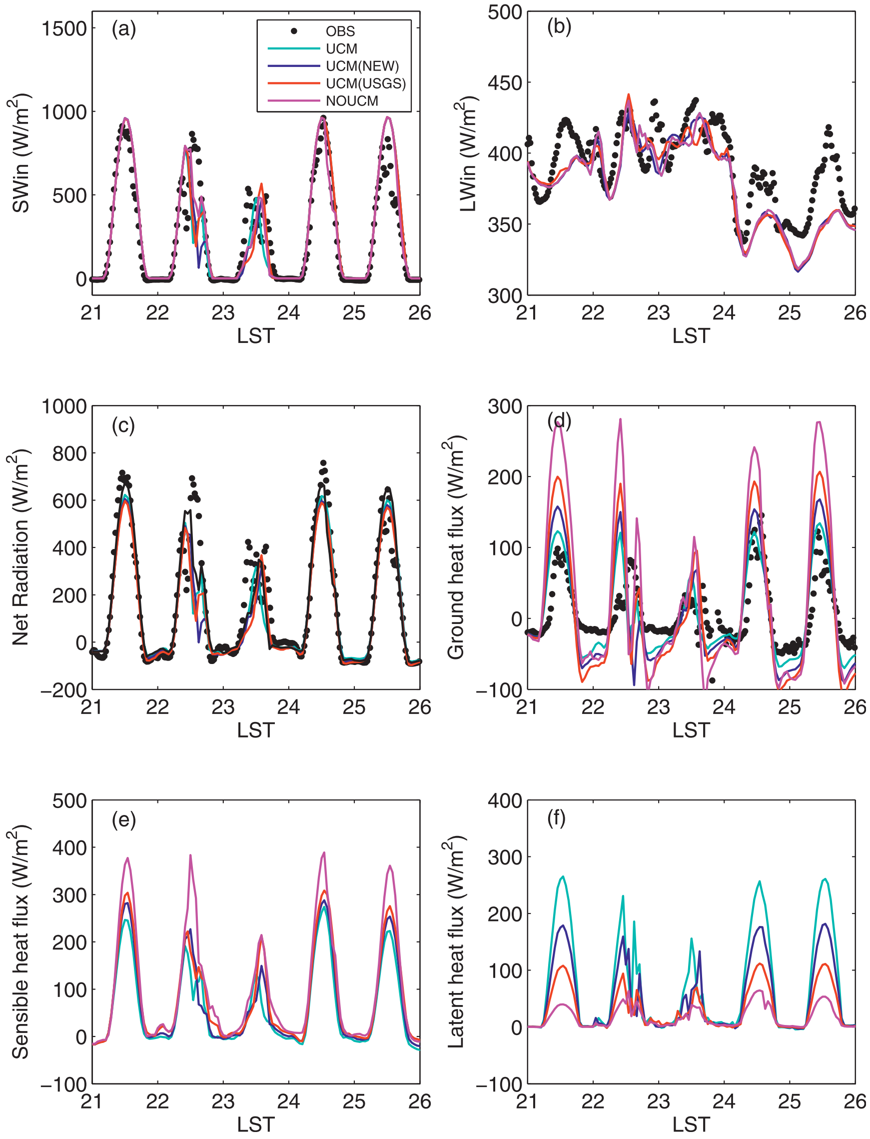

FIG. 3. The surface energy components: (a) incoming shortwave radiation, (b) incoming longwave radiation, (c) net radiation, (d) ground heat flux, (e) sensible heat flux, (f) latent heat flux. The *x* axis is in local standard time (LST) from 21 to 26 Jul 2008. Note that there are no observations for sensible heat flux and latent heat flux.

dataset that accounts for recent urbanization. However, this is due to the fact that the USGS land-cover dataset has only a single urban category and thus produces a higher impervious fraction (90%) in this low-density urban grid cell as compared to the NLCD2006 dataset (50% for using the default UCM and 74% for using the new UCM). This highlights the importance of using a detailed urban surface representation, with multiple urban categories, in analyzing the hydrometeorological and climatic impacts of urbanization.

The simulation using the default UCM captures the daytime variations in ground heat flux better than the other three configurations, followed by the UCM (new) simulation, especially preceding and following the storm period. This highlights the benefits of using a UCM with the more detailed land-cover dataset, compared to a simpler urban representation (e.g., using the traditional approach to calculate urban fluxes or using the USGS land-cover dataset). This is in broad agreement with many studies that have shown a better performance of WRF with a UCM in urban environments (see, e.g., Lee et al. 2011; Zhang et al. 2011). Lee et al. (2011) report that WRF simulations with a UCM are better able to capture the near-surface air temperature and the

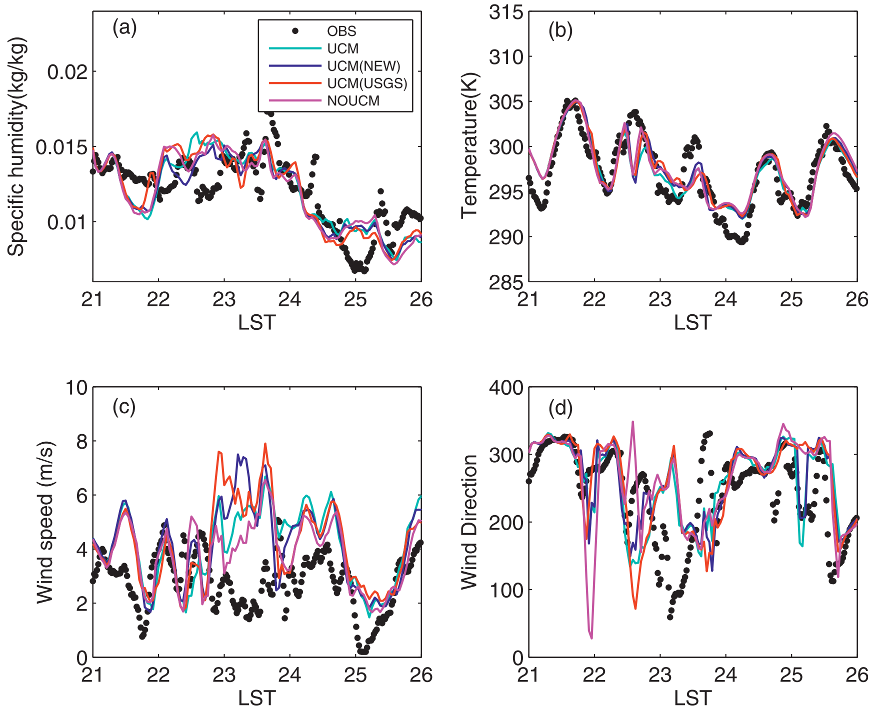

FIG. 4. (a) Specific humidity, (b) air temperature, (c) wind speed, and (d) wind direction measured and simulated at the Cub Hill tower (41.2 m above the ground level). The *x* axis is in LST from 21 to 26 Jul 2008.

atmospheric boundary layer height in urban areas. Zhang et al. (2011) found that a UCM is needed in order to correctly reproduce the land surface temperature patterns or the urban heat island effects. However, we also cautiously note that the measured ground heat flux is a point measurement while the simulated ground heat flux is an average value for the grid cell. As such, the comparison between the new and default UCM based only on the ground heat flux remains inconclusive. We are currently conducting additional analyses using more representative experimental datasets to assess the performance of the new UCM scheme comprehensively.

The surface meteorological conditions are also examined by comparing WRF simulations to the observations at the Cub Hill tower site. As shown in Fig. 4, it is clear that the discrepancies between the WRF results and observations are generally larger during the heavy rainfall period (from 22 July to 24 July). For example, the wind speeds produced by WRF are substantially larger than the measurements. The peak in specific humidity occurred during the late evening of 22 July in WRF simulations but in the middle of the day on 23 July in the observations. This time lag in the peak values of specific humidity between WRF simulations and the observations is related to discrepancies in the wind field. As shown in Fig. 4d, there is a phase error in the wind direction comparison between the WRF simulations and the observations. The southerly winds (from 90° to 270°) occurred earlier in WRF (midday on 22 July) than in the observation (midnight on 22 July to early morning on 23 July). The southerly and southeasterly winds are the main agents for transporting moist air. As a result, the fact that the southerly winds occurred much earlier in WRF simulations causes the peak value in the specific humidity to appear earlier in the WRF simulations than in the observations. For air temperature, WRF performs poorly during rainfall periods. During these periods, the range of air temperatures from WRF is limited compared to the observations, that is, WRF temperature is much colder in the daytime (by up to 8 K) and hotter in the nighttime (by up to 3 K). While the air temperature measurements may have relatively larger uncertainties under heavy rainfall conditions, this discrepancy is more likely to be related to the fact that WRF does not capture rainfall fields correctly, as will be shown later. For example, in the late afternoon on 23 July, WRF started to generate rainfall, which was absent in the observations, and hence, the air temperature in WRF was almost 5 K lower than the observations.

Comparisons of 2-m air temperature and specific humidity measured by ASOS at BWI, NAK, and DMH (locations shown in Fig. 1) showed similarities in the

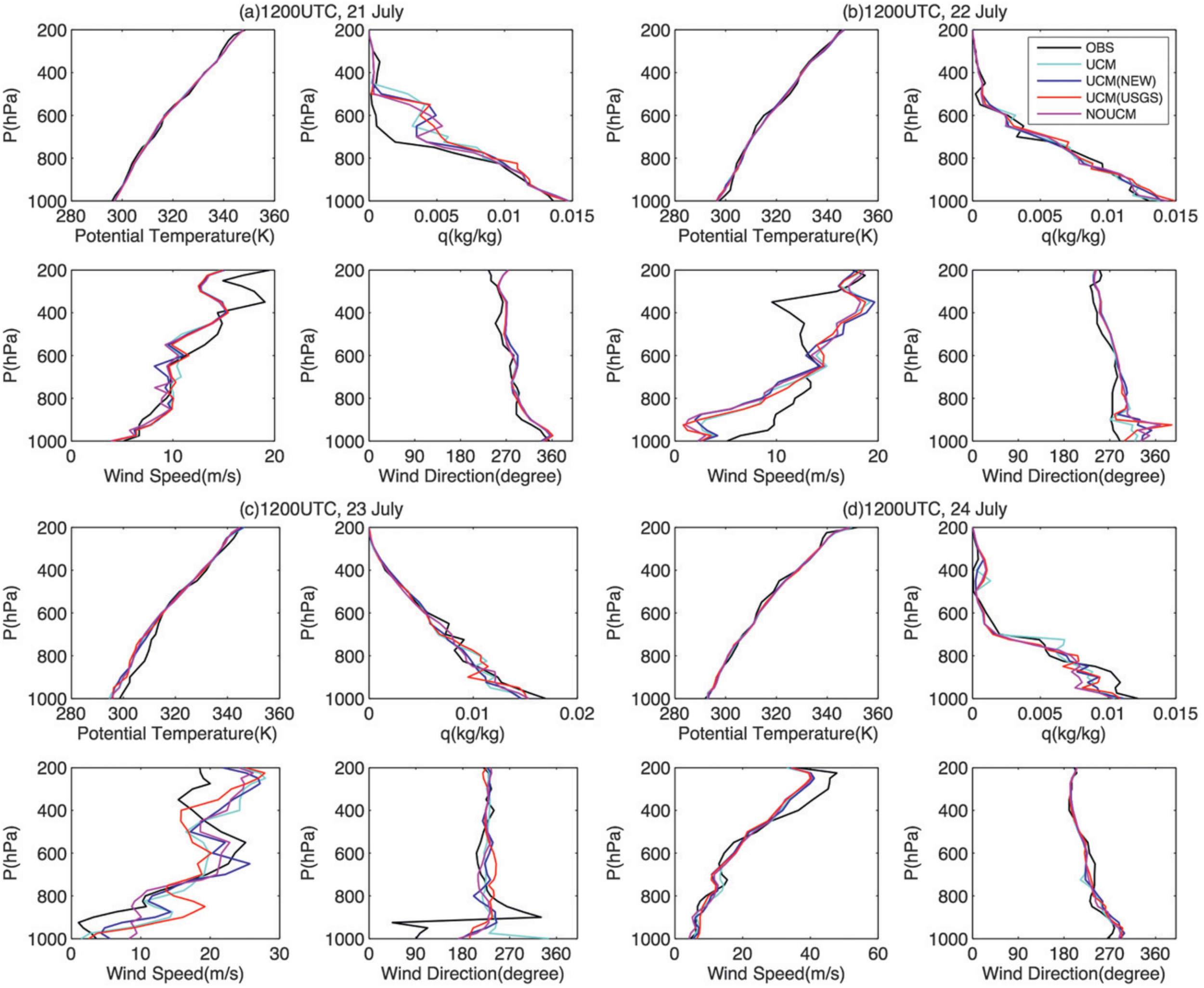

FIG. 5. Vertical profiles of potential temperature, specific humidity, wind speed and wind direction at the APG site during the heavy rainfall period: (a) 21 Jul, (b) 22 Jul, (c) 23 Jul, (d) 24 Jul. Profiles are all at the time of the sounding: 1200 UTC (0700 LST).

magnitudes and timing patterns of errors (not shown here).

b. Vertical atmospheric profiles

In this section, vertical profiles of potential temperature, specific humidity, wind speed, and wind direction from WRF simulations at 1200 UTC (0700 LST) are compared to radiosonde measurements at the APG (in d03) site throughout the rainfall event (from 21 to 24 July). As shown in Fig. 5, it is clear that the vertical profiles of potential temperature, specific humidity, and winds are not highly sensitive to the urban surface representations. The vertical profiles on 21 and 24 July agree well with the measurements (to a lesser extent for specific humidity) since they are less affected by the heavy rainfall event, implying good model skill of WRF under nonrainy conditions. On 22 July, the agreement between the measured and simulated profiles is still good for potential temperature and specific humidity (note that the agreement is even improved for specific humidity in the upper atmosphere as compared to 21 and 24 July), but the errors are large for wind speed and direction. In particular, the jetlike structure at around 700 hPa is missed by all WRF simulations. On 23 July (about 12 h before the heavy rainfall event), all profiles from WRF deviate significantly from the measured ones, especially in the lower atmosphere and especially for winds. The lower part of the atmosphere is drier and colder in WRF simulations. The local maximum in wind speed profile at about 550 hPa is not well reproduced by WRF. Unlike the jetlike structure observed on 22 July, the one formed on 23 July has a much stronger southerly component that brings moisture into the Baltimore region. In addition, the observed winds in the atmospheric

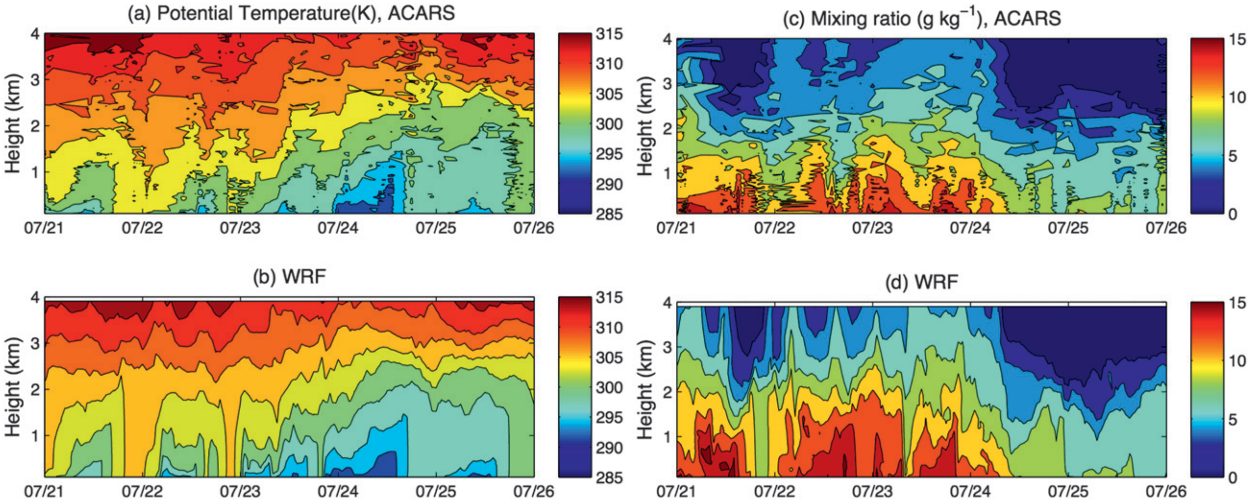

FIG. 6. Evolution of (a),(b) potential temperature and (c),(d) water vapor mixing ratio in the lower atmosphere (up to 4 km above the ground level) at IAD: (a),(c) aircraft measurements and (b),(d) results with the reference WRF simulation (case 1: WSM6 + UCM).

boundary layer (below 850 hPa) on 23 July are easterly and transport moisture from the Atlantic Ocean, while the winds from WRF simulations are southerly or southwesterly. As a result, the discrepancies in the wind fields (both wind speed and wind direction) may result in significant biases in the moisture fields and thus in the simulated rainfall fields.

Fig. 6 compares the potential temperature and water vapor mixing ratio profiles in the lower atmosphere from the reference WRF simulation (case 1) to the ACARS measurements at IAD (d02). Good agreement is seen for potential temperature (Fig. 6a,b), but WRF produces a moister atmospheric boundary layer compared to the ACARS measurements (Fig. 6c,d). Fig. 7 shows

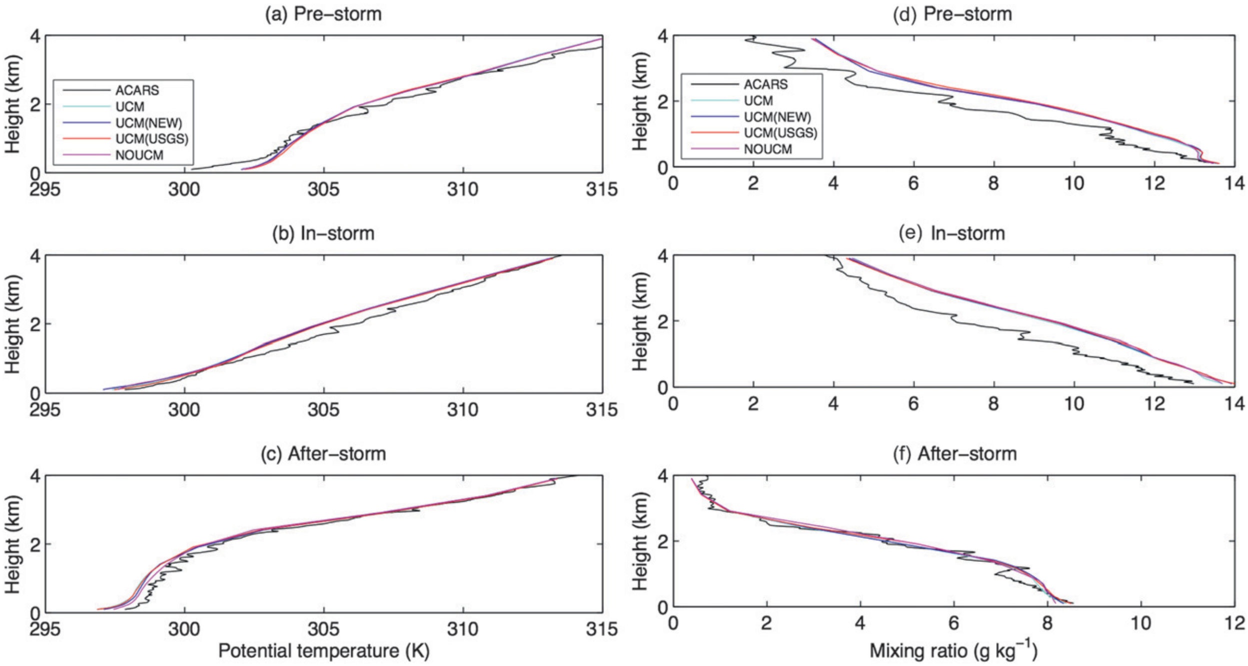

FIG. 7. Composite profiles of (left) potential temperature and (right) water vapor mixing ratio in the lower atmosphere (up to 4 km above the ground level) at IAD: (a),(d) prestorm (0000 UTC 21 Jul to 0000 UTC 22 Jul); (b),(e) in-storm (0000 UTC 22 Jul to 1200 UTC 24 Jul); and (c),(f) after-storm conditions (1200 UTC 24 Jul to 0000 UTC 26 Jul).

the composite profiles of potential temperature and water vapor mixing ratio for the three periods: prestorm, storm, and after storm. It is clear that the composite potential temperature profiles from the WRF simulations match the ACARS measurements better above the atmospheric boundary layer than in the atmospheric boundary layer. The bias is about 1–2 K in the atmospheric boundary layer during the prestorm period. The largest bias occurs at the surface (about 2.5 K) and is caused by the errors in the initial conditions that are taken from NARR. Above the atmospheric boundary, the agreement is very good, except during the storm period when the bias is about 1 K. While the composite temperature profiles from the WRF simulation are in relatively good agreement with the ACARS measurements, the composite water vapor mixing ratio profiles show larger discrepancies. Before and during the storm, the lower atmosphere in the WRF simulations is consistently 1–2 $\mathrm{g\,kg^{-1}}$ moister than the observations. This is consistent with the simulated overestimation of rain at IAD (e.g., compared to the radar observation, as will be shown in Fig. 14). After the storm, the composite water vapor mixing ratio profiles from the WRF simulations correspond to the measured ones, implying that the biases in the water vapor profiles are primarily associated with the initial conditions (provided by NARR) as well as the development of storm conditions.

Different urban surface representations examined in this study do not alter the results significantly, except close to the surface where land–atmosphere exchanges play a significant role. Differences between simulations with different surface parameterizations are an order of magnitude smaller than differences between these WRF runs and observations. These minor differences between simulations with different urban surface representations are largely seen in the atmospheric boundary layer and are connected to the different surface fluxes and rainfall fields generated by the different representations. Similar comparisons (cf. Fig. 6 and Fig. 7) were also conducted at BWI (d03), where only measurements of potential temperature are available. As at IAD, the simulated potential temperature profiles from WRF also match the ACARS measurements at BWI fairly well (not shown here): the bias is larger in the atmospheric boundary layer than above the atmospheric boundary layer, and the largest bias occurs at the surface because of the errors in the initial conditions. The differences between WRF-simulated boundary layer profiles with different urban surface representations are also minor.

The velocity–azimuth display (VAD) wind profiles derived from Doppler velocity measurements at three locations, KLWX, KAKQ, and KCCX, are compared to the WRF-simulated results (the reference simulation, case 1) from d01. Other WRF simulations with different physical parameterizations were also examined and similar features were observed (not shown). KLWX (KAKQ) are located southeast (south) of the Baltimore–Washington metropolitan area (see Fig. 1) and thus are selected to capture the southerly jet flow features in the wind profiles (Figs. 8a,b and Fig. 9). KCCX is located northwest of the Baltimore–Washington metropolitan area and is suitable for identifying errors associated with development of the storm system (Figs. 8c,d and Fig. 10).

A notable feature in the VAD data at KLWX (Figs. 8a,b) is a strong southerly jet ranging from about 500 to 4000 m above the ground that starting on 23 July. The magnitude of the jet is significantly underestimated by the WRF simulation. The low-level jet feature observed in the wind profiles deserves investigation since many studies have demonstrated the role of LLJs in transporting warm, moist air in the lower atmosphere and their close relation with heavy rainfall (Zhang and Fritsch 1986; Stensrud 1996; Higgins et al. 1997; Zhang et al. 2006). According to Zhang et al. (2006), a low-level jet can be broadly defined as a region below 1500 m with wind speeds larger than 12 $\mathrm{m\,s^{-1}}$, positive shear below, and negative shear above. In other words, a local maximum wind speed below 1500 m that is stronger than 12 $\mathrm{m\,s^{-1}}$ can be viewed as an indicator of low-level jets. Fig. 9 shows the maximum wind below 1500 m (above ground level) and its direction at KLWX and KAKQ from the VAD data and the WRF simulation. The horizontal dashed lines in Figs. 9a and 9c show the threshold value of 12 $\mathrm{m\,s^{-1}}$ above which an LLJ is identified. The correlation coefficient, root-mean-square error (RMSE), and mean bias between the WRF-simulated and radar-observed values are shown in Table 2. Note that when calculating these metrics for wind direction, the WRF-simulated or radar-observed values sometimes need to be adjusted (i.e., adding 360°). In general, the WRF simulation captures the variations in the maximum wind speed below 1500 m with correlation coefficients of 0.65 at the two locations. The RMSEs are 2.8 and 2.9 $\mathrm{m\,s^{-1}}$ for KLWX and KAKQ, respectively. The WRF simulation also captures the general variations in the wind direction of the maximum wind speed at KLWX, with the RMSE and the mean bias of 39.5° and 2.8°, respectively. From Figs. 9a and 9b, it is clear that a low-level jet is present in VAD measurements on 23 July at KLWX (the maximum wind speed is above the horizontal dashed line). Its direction is captured in the model simulations, but its strength is underestimated. This is consistent with the comparison in Figs. 8a and 8b. The low-level jet has a southwesterly component (wind direction ranging from 180° to 270°) and thus transports

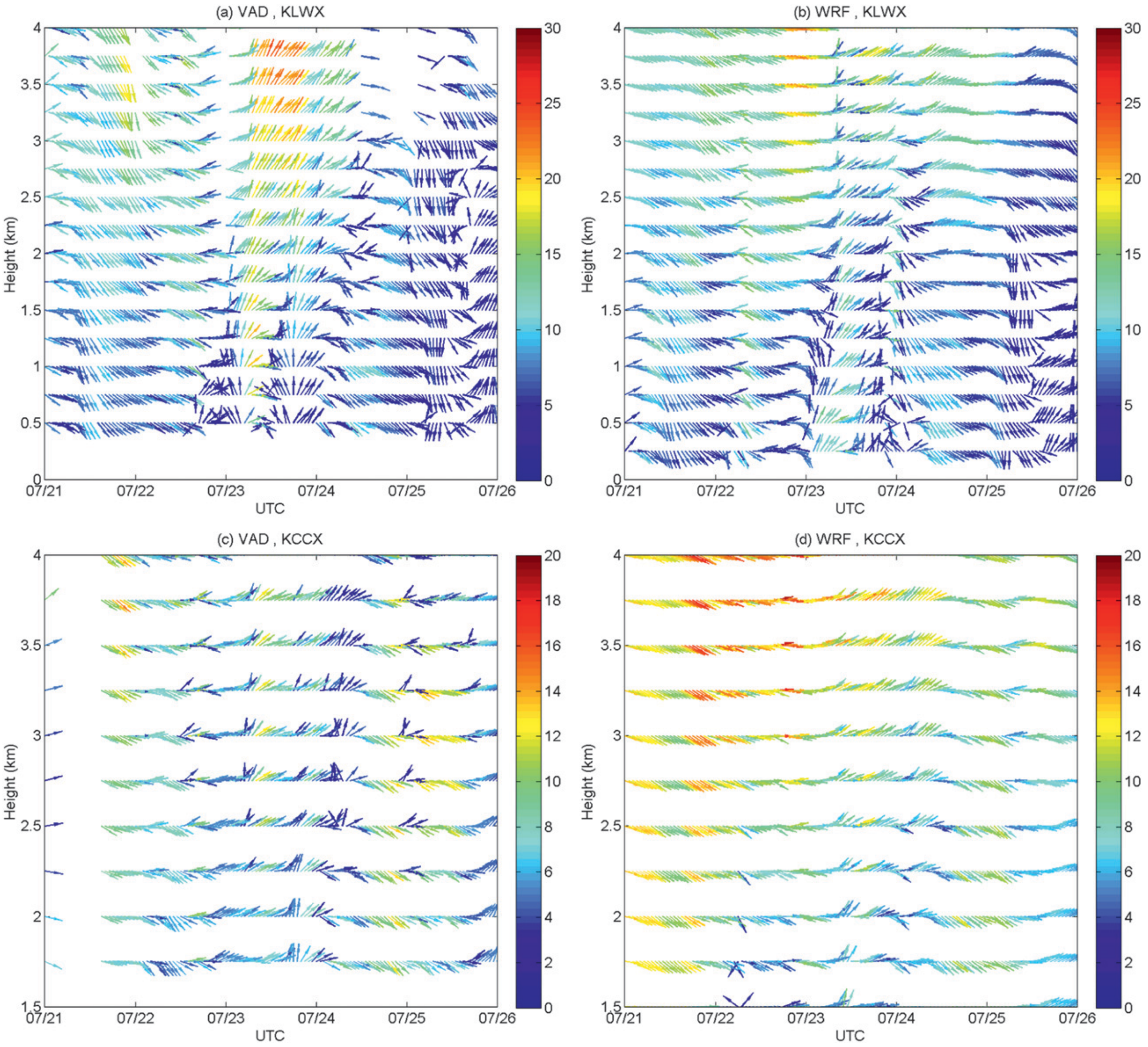

FIG. 8. Horizontal wind speed and direction at (a),(b) KLWX and (c),(d) KCCX in the lower atmosphere from the (a),(c) VAD wind profiles and (b),(d) reference WRF simulation (case 1: WSM6 + UCM). The colors indicate the wind speed magnitude (m s^{-1}) and the arrows are the wind direction in the horizontal plane: *x* axis is the west–east direction while *y* axis is the north–south direction. The heights are above sea level and are at intervals of 250 m.

warmer and moister air from the south to the Baltimore metropolitan area.

The RMSE and the mean bias between the simulated and measured wind direction of the maximum wind speed are roughly twice as large at KAKQ (66.5° and −6.1°, respectively). As can be seen from Figs. 9c and 9d, at KAKQ, two low-level jets are formed, one around 0300 UTC 23 July and the other around 0000 UTC 24 July. The first low-level jet is more significant than the second one, but it is not well reproduced by the WRF simulation with an underestimation of its magnitude and duration. More importantly, the direction associated with this low-level jet is significantly biased by the WRF simulation leading up to the storm period. The observed wind direction veers steadily from about 0000 UTC 22 July to about 1200 UTC 23 July, while the WRF remains roughly constant around 300°. The easterly component (wind direction ranging from 0 to 180°) of the low-level jet is not captured by the WRF simulation, which corresponds with the comparison of radiosonde profiles at APG (Fig. 5c). Note both APG and KAKQ are located along the Chesapeake Bay or the coast. As such, misrepresentation of the easterly low-level jet at these two sites in WRF simulations implies incorrect

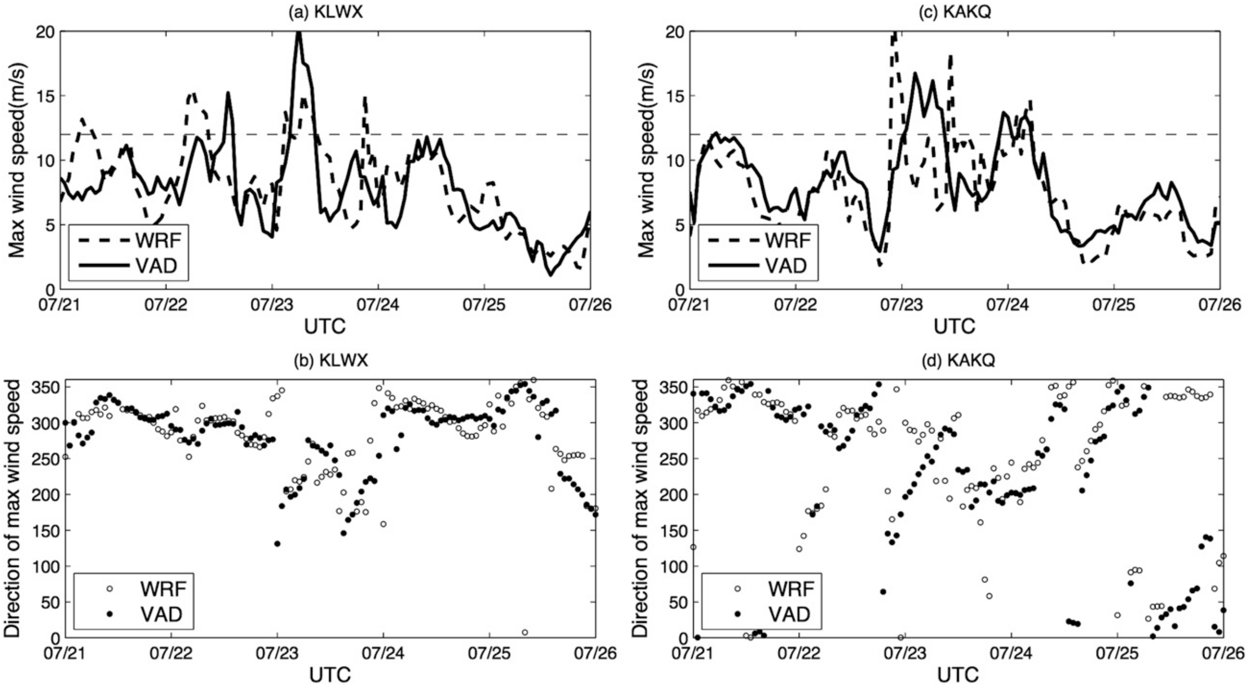

FIG. 9. Comparison of the maximum wind (a),(c) speed and (b),(d) direction below 1500 m (above ground level) at (a),(b) KLWX and (c),(d) KAKQ from VAD data and the reference WRF simulation (case 1: WSM6 + UCM). The horizontal dashed lines in (a),(c) show the threshold value of 12 m s^{-1}.

moisture transport from the Atlantic Ocean, which further results in incorrect rainfall amounts and distribution.

Comparisons of the wind profiles from the model simulation to the VAD data at KCCX (Figs. 8c,d) show that WRF captures the broad features of variation in wind direction. From the composite wind speed and wind direction shown in Fig. 10, it can be seen that before the storm period, the wind is primarily from the

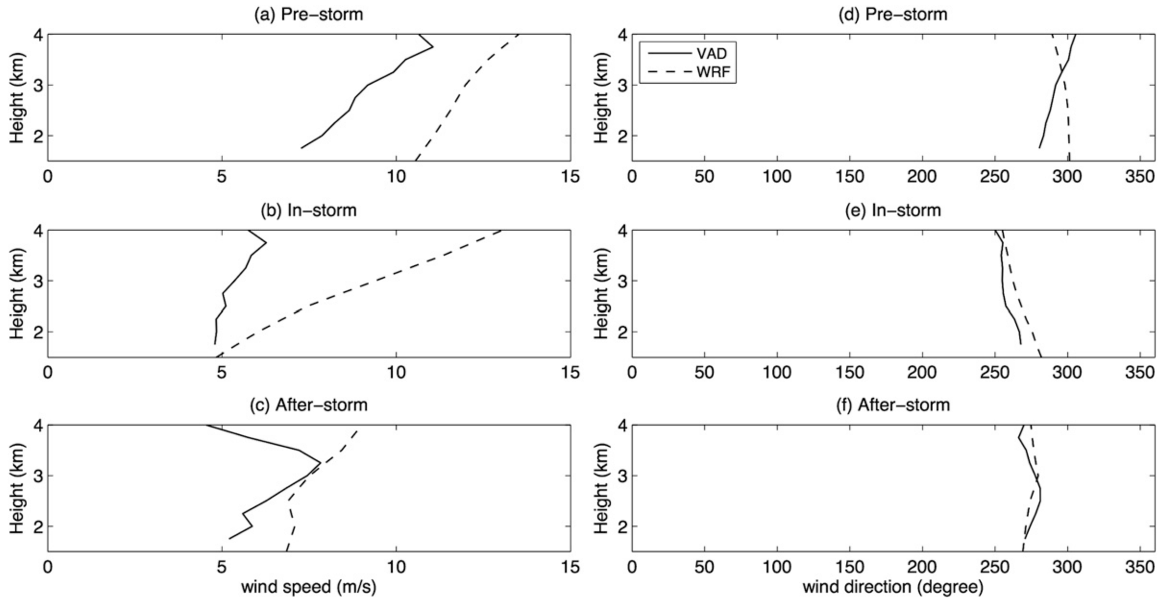

FIG. 10. Composite profiles of wind (a)–(c) speed and (d)–(f) direction at (a),(d) KCCX prestorm (0000 UTC 21 Jul to 0000 UTC 22 Jul); (b),(e) in-storm (0000 UTC 22 Jul to 1200 UTC 24 Jul); and (c),(f) after-storm conditions (1200 UTC 24 Jul to 0000 UTC 26 Jul).

TABLE 2. Comparison between WRF-simulated and radar-observed LLJs.

	Variables	Correlation	RMSE	Mean bias
KLWX	Wind speed	0.65	2.8 m s^{-1}	0.2 m s^{-1}
	Wind direction	0.66	39.5°	2.8°
KAKQ	Wind speed	0.65	2.9 m s^{-1}	−0.7 m s^{-1}
	Wind direction	0.75	66.5°	−6.1°

northwest, while during and after the storm, southerly flows are observed. However, WRF systematically overestimates the wind speed, in particular before the storm and during the storm (Figs. 10b,c). Because KCCX is located to the northwest of Baltimore City, the erroneously large northwesterly winds before the storm period in the model simulation are linked to erroneous rapid motion of the frontal zone toward the Baltimore metropolitan area. As will be seen later, the excessively rapid frontal circulation and movement toward the southeast causes the rainfall event to occur about 4 h ahead of the observations in the Baltimore metropolitan area.

c. Rainfall

In this section, we analyze the biases in WRF-simulated precipitation and link them to the biases in atmospheric dynamics analyzed in the previous section. The rainfall rates simulated by WRF (domain 3), observed by the high-resolution radar dataset, and provided by the coarse-resolution NARR dataset are averaged and compared over their overlap region. As mentioned before, the high-resolution radar rainfall dataset covers a large part of the Baltimore metropolitan area, with a temporal resolution of 15 min and a spatial resolution of 1 km. The NARR dataset covers the whole North American continent, with a temporal resolution of 3 h and a spatial resolution of 32 km. WRF fields from d03 have a temporal resolution of 1 h and a spatial resolution of 1 km. For comparison with WRF, the radar rainfall estimates are averaged into hourly intervals. As can be seen from Fig. 11, the radar observations and the NARR dataset indicates that the rainfall event in d03 started around 0000 UTC 24 July. Note the peak rainfall in the NARR dataset is significantly reduced as compared to the radar observations due to its coarser temporal resolution. It is clear that the WRF simulations do not capture the correct timing of the heavy rainfall event. The rain event simulated by WRF occurred about 4 h earlier than the radar observations. As mentioned earlier, the time lags between WRF simulations and the radar observations are primarily linked to the faster development of the front, which is further illustrated in Fig. 12.

Fig. 12 compares the 2-m specific humidity fields and surface wind fields from the NARR dataset to those from the reference WRF simulation (case 1: WSM6 + UCM) in domain 1 at four times, from 1800 UTC 23 July to 0300 UTC 24 July. As mentioned earlier, the frontal boundary passes the Baltimore–Washington area at 0000 UTC 24 July in the NARR data, as shown by the bold white dotted line in Fig. 12e. Nonetheless, the WRF model fields show that the frontal boundary passed the Baltimore–Washington corridor at 2100 UTC 23 July (Fig. 12d). This is in agreement with the higher (compared to observations) wind speed simulated at KCCX, a location that is behind the front (see Fig. 10). As a result, WRF generates rainfall in the Baltimore metropolitan area approximately 4 h earlier than in the NARR and radar rainfall fields. This feature is similar to the results of Miao et al. (2011) who show that the modeled convergence line in their summer rainfall case

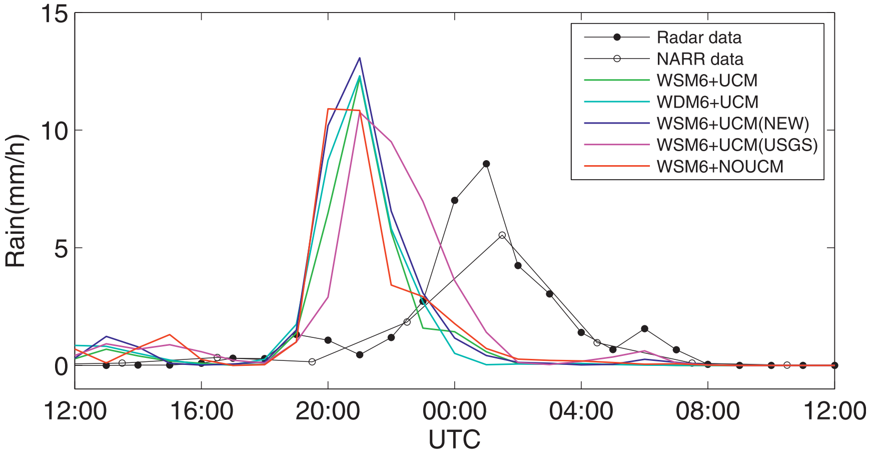

FIG. 11. Time series of rainfall rate averaged over the Baltimore metropolitan area (d03) from 1200 UTC 23 Jul to 1200 UTC 24 Jul.

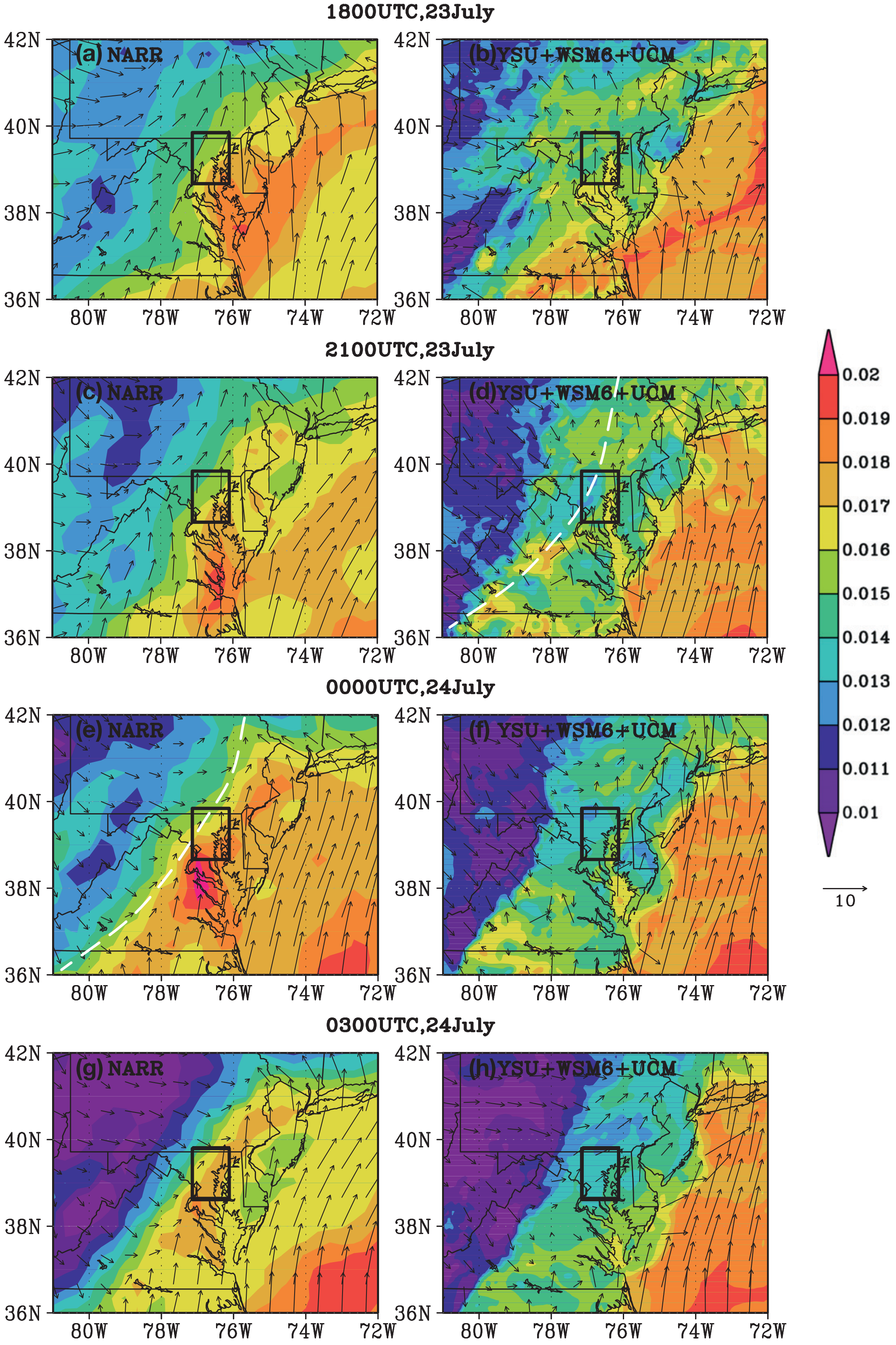

FIG. 12. The 2-m specific humidity (colors) and 10-m winds (arrows) in d01 at: (top row) 1800 and (second row) 2100 UTC on 23 Jul; and (third row) 0000 and (bottom row) 0300 UTC on 24 Jul from NARR and the reference WRF simulation (case 1: WSM6 + UCM). The black square surrounding the Baltimore metropolitan area is d03 in WRF simulations. The bold white dotted lines roughly indicate the frontal boundary locations.

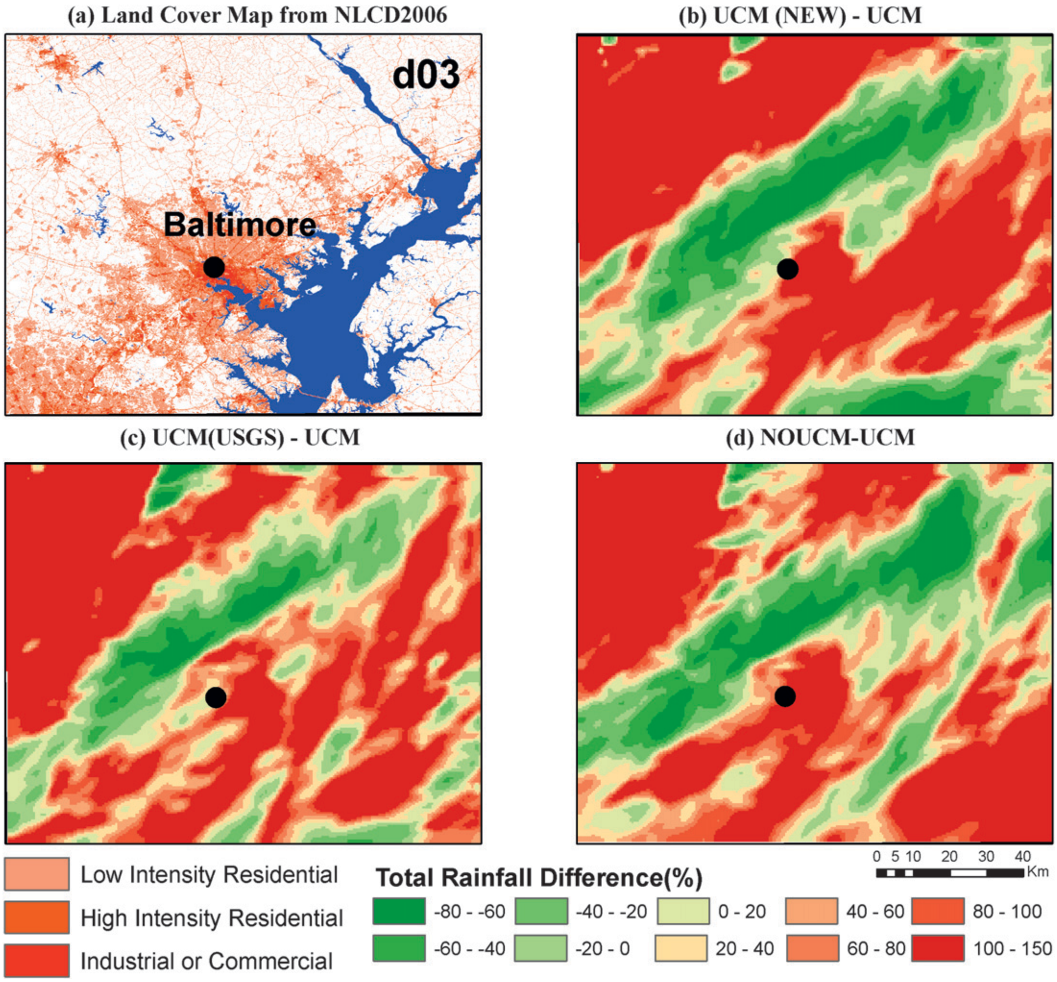

FIG. 13. The sensitivities of total rainfall from 23 to 24 Jul (1200–1200 UTC) in d03 to the urban surface representations in WRF. (a) Land-cover map in d03 and total rainfall difference (%) between: (b) case 3 (new UCM, NLCD2006) and case 1; (c) case 4 (default UCM, USGS) and case 1; and (d) case 5 (no UCM, NLCD2006) and case 1. The reference case 1 uses the default UCM with NLCD2006 dataset. The black dots indicate Baltimore City.

(1 August 2006, Beijing) moves more rapidly than the observed one. Zhang et al. (2009) also observed that the cold front simulated by WRF in their study moves too fast compared with observations. In addition, they also reported that this bias is not alleviated by changing the boundary conditions (i.e., the forcing data).

In addition, the strength of the moisture gradient is significantly different in the WRF simulation than in NARR at the time when the frontal boundary passes the Baltimore area. The cold front generated by the WRF simulation is significantly drier than that in the NARR data. The Chesapeake Bay region also has a lower moisture content, which is consistent with our previous finding that WRF does not capture the easterly flow component that transports moisture from the Atlantic Ocean (as mentioned earlier for comparisons at APG and KAKQ; see Figs. 5c and 9). The lack of an easterly flow along the coast in WRF simulations may also indirectly contribute to the more rapidly moving frontal boundary.

Figure 11 also illustrates the sensitivity of heavy rainfall in WRF to different urban representations and microphysics schemes. The large sensitivity to urban representations is of particular interest. Fig. 13 further illustrates the impact of urban representations on the spatial distribution of total rainfall occurring during 23 and 24 July at a high spatial resolution (1 km). The differences in total rainfall between three cases that use three different urban surface representations (cases 3, 4, and 5 in Table 1) and the control case (case 1 in Table 1) are depicted in Figs. 13b–d. Figure 13a also shows the urban land-use categories in domain 3 from the NLCD2006 date set. As can be seen in Figs. 13b–d, changes in urban surface representations (including

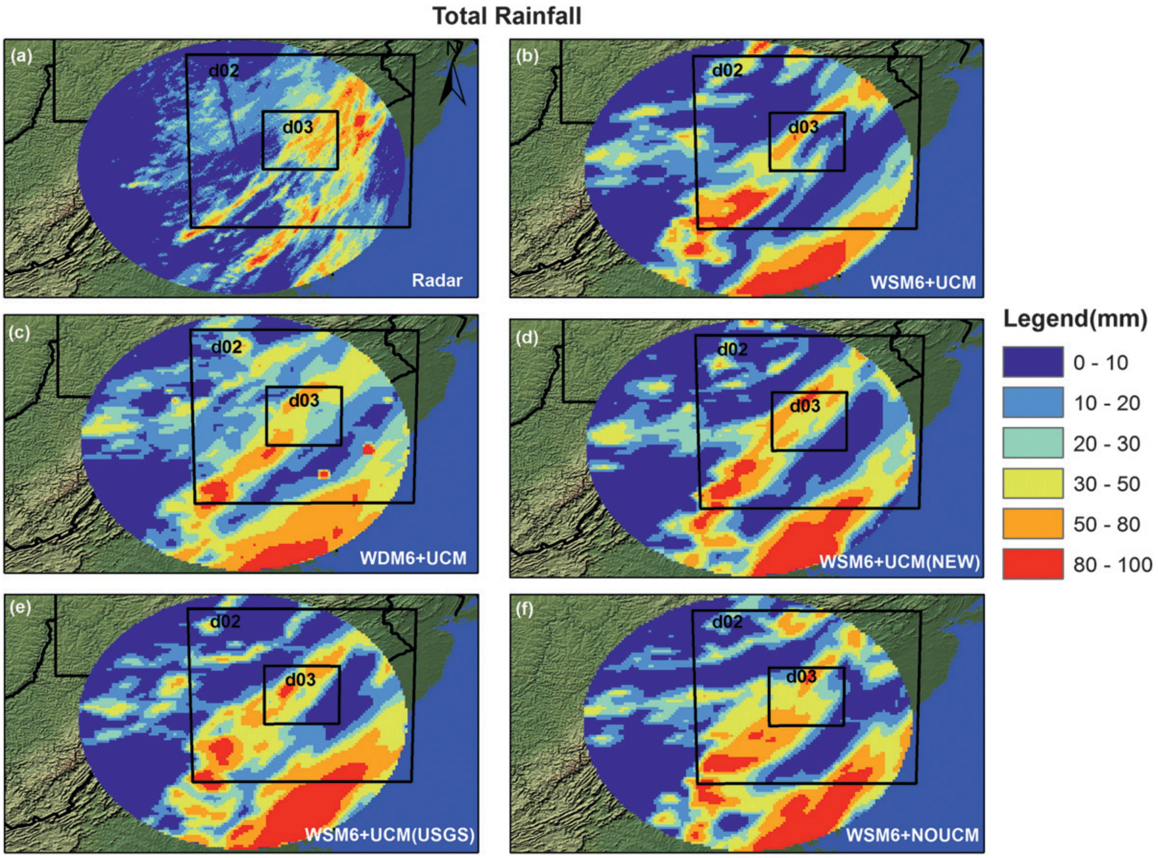

FIG. 14. The total rainfall from 23 to 24 Jul (1200–1200 UTC) (a) measured by the KLWX radar and (b)–(f) produced by WRF simulations with different microphysics and urban surface representations as indicated in the lower right corner of each panel.

changes in the urban flux calculation methods and changes in the land-cover datasets) can result in local differences in total rainfall of more than 150%. The main difference is that the impervious surface fraction and the vegetated surface fraction differ as a result of land-use dataset and UCM selection. For example, a large part of suburban areas around Baltimore and Washington are classified as low-intensity urban land and, thus, a 50% impervious surface fraction is assigned for each grid in the default UCM. In the new UCM, the fraction of impervious surface is calculated directly from NLCD2006, and it tends to exceed 50% around the two cities. The USGS dataset–based run will treat all urban areas as high density with 90% impervious fraction. When no UCM is used, all of the urban areas will be treated exclusively as impervious surfaces. As the impervious surface fraction increases, more available energy is converted into sensible heat flux, which leads to changes in local convection regimes. As the impervious surface fraction increases, more rainfall is generated along the Baltimore–Washington corridor in response to the increases in the sensible heat fluxes, while a belt with reduced rain is produced to the northwest of the urban areas (Fig. 13).

Figure 14 shows the total rainfall from 23 to 24 July (1200–1200 UTC) derived from the KLWX radar and produced by different WRF simulations over a large domain in order to illustrate the sensitivities of large-scale rainfall patterns to microphysics and urban surface representations. From the radar measurement, it is clear that most of the rain is concentrated northeast of the Baltimore metropolitan region (downwind of the urban region; see Smith et al. 2012). Observational studies that have focused on the impact of urbanization on precipitation have shown that warm seasonal rainfall consistently shows a local maximum downwind of major cities [see Shephard (2005) for a review and Smith et al. (2012) for analyses in the Baltimore region]. However, WRF does not generate the maximum rainfall at the correct location for this event. Based on the previous analyses, this is caused by the biases in the WRF-simulated wind fields, which further leads to biases in the moisture transport. The maximum rainfall in WRF simulations occur more inland as compared to the radar observation, which is in agreement with the weaker easterly flow along the Chesapeake Bay or the coast that was observed in section 3b. The faster-moving frontal boundary toward the southeast also contributes to changes in the maximum rainfall location in WRF simulations. In addition, WRF simulations produce the two parallel line structures in the rainfall fields, but generate too much rainfall in each line. This overestimation of rainfall by WRF is also in agreement with many previous studies (see, e.g., Yeung et al. 2011) and is also caused by incorrect moisture transport. Changes in microphysics schemes alter the spatial structure of the rainfall field, but more sophisticated microphysics parameterizations (WDM6) do not generate better results as compared to radar observations.

It is interesting to observe from Fig. 14 that the large-scale rainfall fields are clearly as sensitive to the urban surface representations as to the microphysics schemes. The fact that large-scale rainfall fields are affected by urban surface representations suggests a potentially significant role of urbanization in modifying regional precipitation patterns. More importantly, it also suggests that studies using numerical tools such as WRF to investigate the impact of urbanization on precipitation need to be more careful in selecting urban surface representations. In addition, the significant sensitivity of rainfall structure to urban surface representations observed in our study demonstrates a strong need for accurate characterizations of urban surfaces in numerical weather prediction models.

4. Conclusions

In this study, we examine the role of land surface processes in modulating heavy rainfall in the Baltimore–Washington metropolitan region and the role of heavy rainfall in controlling land surface processes and the structure of the atmospheric boundary layer. Analyses are based on comparisons of high-resolution WRF model fields with a broad range of observations. The performance of WRF and sensitivities to urban surface parameterizations and microphysics schemes are examined. The main conclusions are as follows:

1) The urban surface representation is a key determinant of the surface energy balance in urban environment. The UCM with the high-resolution NLCD2006 land-cover dataset captures the surface energy partitioning reasonably well at the Cub Hill tower site (a low-density residential area). The UCM with the default USGS land-cover dataset case and the no-UCM case, which have higher impervious fractions, yield larger sensible and ground heat fluxes and smaller latent heat fluxes compared to the control simulation. As the urban surface representation more accurately reflects the vegetated/impervious fractions, the calculation of land–atmosphere exchanges becomes more accurate, yet it remains inconclusive whether adding grid-scale complexity via the new UCM yields further improvement.
2) The surface microclimate conditions are generally well reproduced by WRF. During the rainfall period, however, WRF generates large biases in air temperature, specific humidity, and the wind field. These biases are closely associated with the discrepancies in the WRF-modeled rainfall field such as the overestimation of the inland rainfall and the incorrect timing of the rainfall event.
3) Large biases are observed in the WRF-simulated wind field in the lower atmosphere: WRF simulations do not fully capture the jetlike structures that are main agents for moisture transport. WRF simulations also produce stronger northwesterly winds that move the frontal boundary faster than in the observations. The agreement between WRF-simulated and measured vertical profiles is good for potential temperature and specific humidity preceding and following the heavy rainfall period, but less satisfactory during the storm when the simulated atmospheric boundary layer is considerably moister than the observed one.
4) WRF simulations reproduce the inland linear patterns of rainfall but generate too much precipitation along these lines and not enough precipitation elsewhere, particularly farther downwind of the urban areas (along the Chesapeake Bay). In addition, WRF does not capture the correct timing for the passage of the frontal system, which results in a time lag between the simulated and observed rainfall fields.
5) Both urban surface representations and microphysics schemes in WRF affect heavy rainfall modeling significantly. In particular, the sensitivity of spatial rainfall structures and the spatially averaged time series of rainfall rate to urban surface representation are comparable to the sensitivity to the microphysics scheme examined in our study, demonstrating that inclusion of urban physics is important for WRF and other numerical weather prediction models to capture heavy rainfall.

The significant role of urban surface representations in modulating urban-atmosphere exchanges, atmospheric boundary layer structures, and rainfall distribution has many implications. First, it demonstrates the importance of developing an urban modeling system that captures the key finescale processes that occur in urban environments and coupling it to the large-scale numerical weather and climate models (Chen et al. 2011). Second, it suggests that choice of urban representation in the WRF model, like the choice of any other physical parameterization, plays a significant role in rainfall modeling. Studies that rely on numerical tools such as WRF to assess the impact of urbanization on rainfall need to give careful consideration to the choice of urban surface representation.

The current study does have some limitations that are important to appreciate. First of all, the conclusions are drawn based on analyses of a single heavy-rainfall event. More precipitation events of different types and under different forcing conditions should be investigated to overcome the limitation of a case study. Second, some analyses such as the validation of surface radiative and turbulent fluxes are based on limited measurements. More experimental datasets will be used in future work to assess the performance of different urban surface representations. In addition, some of the biases observed in this study are not isolated from the uncertainties in the initial and boundary conditions, which were provided by the NARR dataset. Future work involves using other forcing datasets in addition to NARR to help identify the biases that are generated by WRF itself. This paper also identifies several limitations in the WRF modeling system that improvements to the urban parameterization may not address, such as the biases in the WRF wind fields that cause a faster development of the front. Further efforts are also needed to address these limitations in order to improve the predictability of WRF at large and to use WRF for other environmental and hydrological applications.

Acknowledgments. This work is supported by the NSF under Grant CBET-1058027 and by the Mid-Infrared Technology for Health and the Environment (MIRTHE) NSF Engineering Research Center at Princeton University under Grant EEC-0540832. The simulations were performed on the supercomputing clusters of the National Center for Atmospheric Research and of Princeton University. We are grateful to Drs. John Hom and Nicanor Saliendra from the Forest Service of the U.S. Department of Agriculture for providing us with the mean meteorological observations from the Cub Hill tower. We also thank Yinzhen Jin and Long Yang for their help in processing the VAD data and Ting Sun for processing the figures.

REFERENCES

Ashley, W. S., M. L. Bentley, and J. A. Stallins, 2012: Urban-induced thunderstorm modification in the southeast United States. *Climatic Change,* **113,** 481–498.

Betts, A. K., J. H. Ball, A. C. M. Beljaars, M. J. Miller, and P. A. Viterbo, 1996: The land surface-atmosphere interaction: A review based on observational and global modeling perspectives. *J. Geophys. Res.,* **101,** 7209–7225.

Bornstein, R., and Q. L. Lin, 2000: Urban heat islands and summertime convective thunderstorms in Atlanta: Three case studies. *Atmos. Environ.,* **34,** 507–516.

Brutsaert, W., 2005: *Hydrology: An introduction.* Cambridge University Press, 605 pp.

Chen, F., and Coauthors, 2011: The integrated WRF/urban modelling system: Development, evaluation, and applications to urban environmental problems. *Int. J. Climatol.,* **31,** 273–288.

Dixon, P. G., and T. L. Mote, 2003: Patterns and causes of Atlanta's urban heat island-initiated precipitation. *J. Appl. Meteor.,* **42,** 1273–1284.

Higgins, R. W., Y. Yao, E. S. Yarosh, J. E. Janowiak, and K. C. Mo, 1997: Influence of the Great Plains low-level jet on summertime precipitation and moisture transport over the central United States. *J. Climate,* **10,** 481–507.

Hong, S. Y., and J. J. Lim, 2006: The WRF Single-Moment 6-Class Microphysics Scheme (WSM6). *J. Korean Meteor. Soc.,* **42,** 129–151.

——, K. S. Lim, Y. H. Lee, J. C. Ha, H. W. Kim, S. J. Ham, and J. Dudhia, 2010: Evaluation of the WRF Double-Moment 6-Class Microphysics Scheme for Precipitating Convection. *Adv. Meteor.,* **2010,** 707253, doi:10.1155/2010/707253.

Jankov, I., W. A. Gallus, M. Segal, B. Shaw, and S. E. Koch, 2005: The impact of different WRF model physical parameterizations and their interactions on warm season MCS rainfall. *Wea. Forecasting,* **20,** 1048–1060.

Jiang, X. Y., C. Wiedinmyer, F. Chen, Z. L. Yang, and J. C. F. Lo, 2008: Predicted impacts of climate and land use change on surface ozone in the Houston, Texas, area. *J. Geophys. Res.,* **113,** D20312, doi:10.1029/2008JD009820.

Jin, M. L., and J. M. Shepherd, 2008: Aerosol relationships to warm season clouds and rainfall at monthly scales over east China: Urban land versus ocean. *J. Geophys. Res.,* **113,** D24S90, doi:10.1029/2008JD010276.

——, ——, and W. Z. Zheng, 2010: Urban surface temperature reduction via the urban aerosol direct effect: A remote sensing and WRF model sensitivity study. *Adv. Meteor.,* **2010,** 681587, doi:10.1155/2010/681587.

Krajewski, W. F., and Coauthors, 2011: Towards better utilization of NEXRAD data in hydrology: An overview of Hydro-NEXRAD. *J. Hydroinformatics,* **13,** 255–266.

Lee, S. H., and Coauthors, 2011: Evaluation of urban surface parameterizations in the WRF model using measurements during the Texas Air Quality Study 2006 field campaign. *Atmos. Chem. Phys.,* **11,** 2127–2143.

Lim, K. S. S., and S. Y. Hong, 2010: Development of an effective double-moment cloud microphysics scheme with prognostic cloud condensation nuclei (CCN) for weather and climate models. *Mon. Wea. Rev.,* **138,** 1587–1612.

Lin, C. Y., W. C. Chen, P. L. Chang, and Y. F. Sheng, 2011: Impact of the urban heat island effect on precipitation over a complex geographic environment in northern Taiwan. *J. Appl. Meteor. Climatol.,* **50,** 339–353.

Loose, T., and R. D. Bornstein, 1977: Observations of mesoscale effects on frontal movement through an urban area. *Mon. Wea. Rev.,* **105,** 563–571.

Miao, S. G., F. Chen, Q. C. Li, and S. Y. Fan, 2011: Impacts of urban processes and urbanization on summer precipitation: A case study of heavy rainfall in Beijing on 1 August 2006. *J. Appl. Meteor. Climatol.,* **50,** 806–825.

Niyogi, D., and Coauthors, 2011: Urban modification of thunderstorms: An observational storm climatology and model case study for the Indianapolis urban region. *J. Appl. Meteor. Climatol.,* **50,** 1129–1144.

Ntelekos, A. A., J. A. Smith, and W. F. Krajewski, 2007: Climatological analyses of thunderstorms and flash floods in the Baltimore metropolitan region. *J. Hydrometeor.,* **8,** 88–101.

——, ——, M. L. Baeck, W. F. Krajewski, A. J. Miller, and R. Goska, 2008: Extreme hydrometeorological events and the urban environment: Dissecting the 7 July 2004 thunderstorm over the Baltimore MD metropolitan region. *Water Resour. Res.,* **44,** W08446, doi:10.1029/2007WR006346.

——, ——, L. Donner, J. D. Fast, W. I. Gustafson, E. G. Chapman, and W. F. Krajewski, 2009: The effects of aerosols on intense convective precipitation in the northeastern United States. *Quart. J. Roy. Meteor. Soc.,* **135,** 1367–1391.

Pielke, R. A., 2001: Influence of the spatial distribution of vegetation and soils on the prediction of cumulus convective rainfall. *Rev. Geophys.,* **39,** 151–177.

Rosenfeld, D., 2000: Suppression of rain and snow by urban and industrial air pollution. *Science,* **287,** 1793–1796.

Shem, W., and M. Shepherd, 2009: On the impact of urbanization on summertime thunderstorms in Atlanta: Two numerical model case studies. *Atmos. Res.,* **92,** 172–189.

Shephard, J. M., 2005: A review of current investigations of urban-induced rainfall and recommendations for the future. *Earth Interact.,* **9.** [Available online at http://EarthInteractions.org.]

Shepherd, J. M., M. Carter, M. Manyin, D. Messen, and S. Burian, 2010: The impact of urbanization on current and future coastal precipitation: a case study for Houston. *Environ. Plann.,* **37B,** 284–304.

Skamarock, W. C., and J. B. Klemp, 2008: A time-split nonhydrostatic atmospheric model for weather research and forecasting applications. *J. Comput. Phys.,* **227,** 3465–3485.

Smith, J. A., M. L. Baeck, G. Villarini, C. Welty, A. J. Miller, and W. F. Krajewski, 2012: Analyses of a long-term, high-resolution radar rainfall data set for the Baltimore metropolitan region. *Water Resour. Res.,* **48,** W04504, doi:10.1029/2011WR010641.

Stensrud, D. J., 1996: Importance of low-level jets to climate: A review. *J. Climate,* **9,** 1698–1711.

Talbot, C., E. Bou-Zeid, and J. Smith, 2012: Nested mesoscale large-eddy simulations with WRF: Performance in real test cases. *J. Hydrometeor.,* **13,** 1421–1441.

Trier, S. B., F. Chen, and K. W. Manning, 2004: A study of convection initiation in a mesoscale model using high-resolution land surface initial conditions. *Mon. Wea. Rev.,* **132,** 2954–2976.

——, ——, ——, M. A. LeMone, and C. A. Davis, 2008: Sensitivity of the PBL and precipitation in 12-day simulations of warm-season convection using different land surface models and soil wetness conditions. *Mon. Wea. Rev.,* **136,** 2321–2343.

——, M. A. LeMone, F. Chen, and K. W. Manning, 2011: Effects of surface heat and moisture exchange on ARW-WRF warm-season precipitation forecasts over the central United States. *Wea. Forecasting,* **26,** 3–25.

Wang, Z. H., E. Bou-Zeid, S. K. Au, and J. A. Smith, 2011: Analyzing the sensitivity of WRF's single-layer urban canopy model to parameter uncertainty using advanced Monte Carlo simulation. *J. Appl. Meteor. Climatol.,* **50,** 1795–1814.

——, ——, and J. A. Smith, 2013: A coupled energy transport and hydrological model for urban canopies evaluated using a wireless sensor network. *Quart. J. Roy. Meteor. Soc.,* doi:10.1002/qj.2032, in press.

Wood, E. F., and Coauthors, 2011: Hyperresolution global land surface modeling: Meeting a grand challenge for monitoring Earth's terrestrial water. *Water Resour. Res.,* **47,** W05301, doi:10.1029/2010WR010090.

Wright, D. B., J. A. Smith, G. Villarini, and M. L. Baeck, 2012: Hydroclimatology of flash flooding in Atlanta. *Water Resour. Res.,* **48,** W04524, doi:10.1029/2011WR011371.

Yeung, J. K., J. A. Smith, G. Villarini, A. A. Ntelekos, M. L. Baeck, and W. F. Krajewski, 2011: Analyses of the warm season rainfall climatology of the northeastern US using regional climate model simulations and radar rainfall fields. *Adv. Water Resour.,* **34,** 184–204.

Zhang, D. L., and J. M. Fritsch, 1986: Numerical simulation of the meso-β scale structure and evolution of the 1977 Johnstown Flood. Part I: Model description and verification. *J. Atmos. Sci.,* **43,** 1913–1943.

——, S. L. Zhang, and S. J. Weaver, 2006: Low-level jets over the Mid-Atlantic states: Warm-season climatology and a case study. *J. Appl. Meteor. Climatol.,* **45,** 194–209.

——, Y. X. Shou, R. R. Dickerson, and F. Chen, 2011: Impact of upstream urbanization on the urban heat island effects along the Washington–Baltimore corridor. *J. Appl. Meteor. Climatol.,* **50,** 2012–2029.

Zhang, Y., J. A. Smith, A. A. Ntelekos, M. L. Baeck, W. F. Krajewski, and F. Moshary, 2009: Structure and evolution of precipitation along a cold front in the northeastern United States. *J. Hydrometeor.,* **10,** 1243–1256.